JACS
JOURNAL OF THE AMERICAN CHEMICAL SOCIETY

Article

pubs.acs.org/JACS

Thermodynamically Driven One-Dimensional Evolution of Anatase TiO_2 Nanorods: One-Step Hydrothermal Synthesis for Emerging Intrinsic Superiority of Dimensionality

Jiazang Chen, Hong Bin Yang, Jianwei Miao, Hsin-Yi Wang, and Bin Liu*

Division of Chemical and Biomolecular Engineering, School of Chemical and Biomedical Engineering, Nanyang Technological University, 62 Nanyang Drive, Singapore 637459, Singapore

Supporting Information

ABSTRACT: In photoelectrochemical cells, there exists a competition between transport of electrons through the porous semiconductor electrode toward the conducting substrate and back-reaction of electrons to recombine with oxidized species on the semiconductor−electrolyte interface, which determines the charge collection efficiency and is strongly influenced by the density and distribution of electronic states in band gap and architectures of the semiconductor electrodes. One-dimensional (1D) anatase TiO_2 nanostructures are promising to improve charge transport in photoelectrochemical devices. However, the conventional preparation of 1D anatase nanostructures usually steps via a titanic acid intermediate (e.g., $H_2Ti_3O_7$), which unavoidably introduces electronic defects into the host lattice, resulting in undesired shielding of the intrinsic role of dimensionality. Here, we manage to promote the 1D growth of anatase TiO_2 nanostructures by adjusting the growth kinetics, which allows us to grow single-crystalline anatase TiO_2 nanorods through a one-step hydrothermal reaction. The synthesized anatase nanorods possess a lower density of trap states and thus can simultaneously facilitate the diffusion-driven charge transport and suppress the electron recombination. Moreover, the electronically boundary free nanostructures significantly enhance the trap-free charge diffusion coefficient of the anatase nanorods, which enables the emergence of the intrinsic superiority of dimensionality. By virtue of these merits, the anatase nanorods synthesized in this work take obvious advantages over the conventional anatase counterparts in photoelectrochemical systems (e.g., dye-sensitized solar cells) by showing more efficient charge transport and collection and higher energy conversion efficiency.

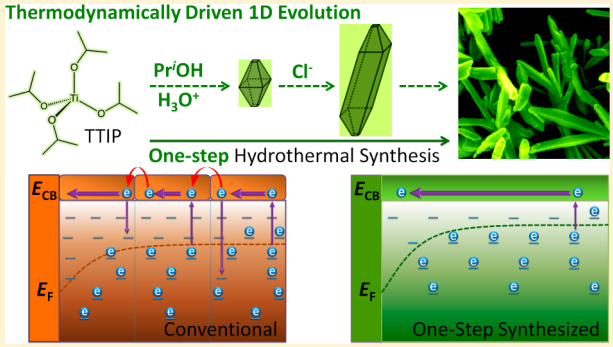

INTRODUCTION

Semiconductor nanostructures are of both theoretical and technological importance and exhibit a wide range of electrical and optical properties that can offer widespread applications in photocatalysis, solar energy conversion, energy storage, etc.[1−4] Among them, nanocrystalline TiO_2 is one of the most studied semiconductor nanostructures.[5−7] As motivated by the pioneering work of hydrogen generation through water photoelectrolysis and the development of efficient dye-sensitized solar cells (DSSCs),[8−10] considerable research efforts have been devoted to synthesize TiO_2 nanostructures for efficient photoelectrochemical applications.[11−13]

The photoelectrochemical performance of semiconductor nanostructures including TiO_2 has a strong dimensionality dependence. It has been suggested that 1D nanostructures, such as hollow nanotubes and solid nanorods, are beneficial for charge transport by building a central conducting path to contact the conducting substrate and prevent charge recombination by forming surface band bending in the radial direction.[14] With DSSC as an example, since the electron collection efficiency and overall energy conversion efficiency are mainly determined by the competition between the transport of electrons through the porous semiconductor electrode and the recombination of electrons with I_3^- ions on the semiconductor−electrolyte interface (SEI), cells with 1D TiO_2 nanostructures would theoretically possess better photovoltaic performance.[14] Anatase TiO_2 nanostructures usually exhibit superior performance over the rutile counterparts in photoelectrochemical systems such as DSSCs,[15,16] due to the facile charge transport and efficient separation of light-induced electron−hole pairs. However, the formation of anatase nanostructures usually involves complex and laborious steps.

Generally, 1D anatase nanostructures can be synthesized via anodization of metallic titanium foil or hydrothermal treatment of the TiO_2 precursor in concentrated alkali-metal hydroxide solution. During the synthesis, the nanostructures undergo multiple stages of intercalation and deintercalation of guest ions into and from the crystal lattice. These intercalation processes would swell and distort the original crystal lattice, which could

Received: August 6, 2014
Published: October 7, 2014

   dx.doi.org/10.1021/ja5080568 | J. Am. Chem. Soc. 2014, 136, 15310−15318

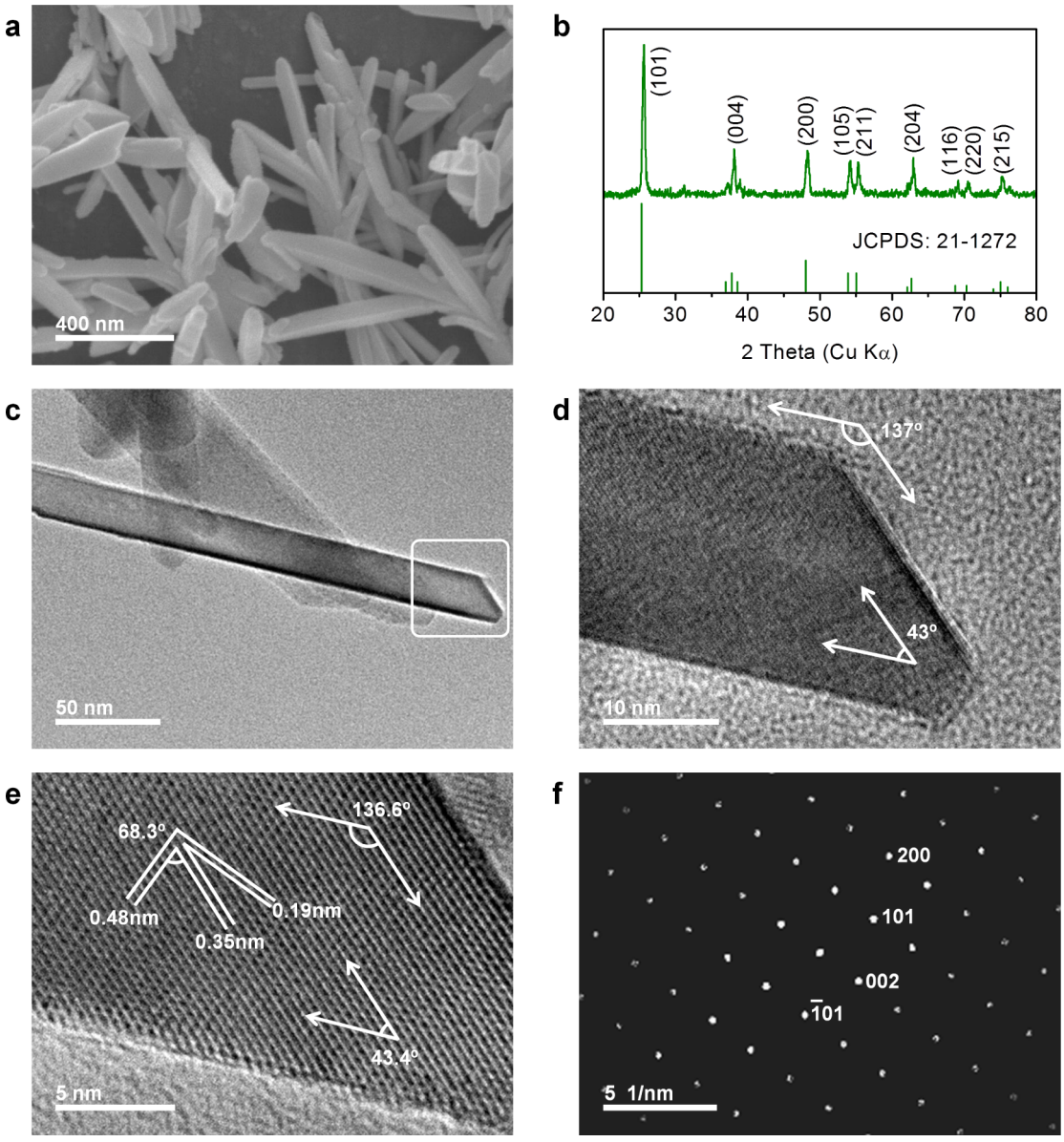

Figure 1. (a) FESEM image, (b) XRD pattern, (c, d) TEM images, (e) HRTEM image, and (f) SAED pattern of TiO_2 nanorods prepared by hydrothermal treatment of 0.2 mL of TTIP in a solution containing 10 mL of ammonia, 8 mL of isopropyl alcohol, and 0.8 g of NH_4Cl at 170 °C for 72 h.

not be perfectly recovered even after the removal of guest ions.[17] Moreover, a phase transformation simultaneously occurred along with the multiple (de)intercalation processes.[18,19] Thus, a very high density of defects would be formed during these multiple (de)intercalation processes, which could act as charge traps in the photoelectrochemical system. A high density of trap states in the band gap of the semiconductor will prolong the transport time of charges in the electrodes by increasing the probability of trapping/detrapping events, resulting in a lowering of charge diffusion coefficient.[14,20] All of these lead to undesired shielding of the intrinsic superiority of dimensionality in 1D anatase nanostructures. For example, it has been reported that the transport of charge is only marginally fast in 1D TiO_2 nanostructures, even in vertically oriented arrays, in comparison with the particulate counterparts, due to the large density of traps.[20] In addition, the trap states located at/near the surface of the semiconductor electrode will act as intermediates to trap electrons and increase the probability of charge recombination. The severe leakage of charges via the surface states not only reduces the charge collection efficiency but also results in a lowering of voltage output. To bring out the potential of the superiority of the nanostructures, it is of great importance to propose feasible approaches for the growth of 1D anatase TiO_2 nanostructures.

In the present work, we successfully synthesize 1D single-crystalline anatase TiO_2 nanorods (denoted AlAR) by the one-step hydrothermal treatment of titanium tetraisopropoxide (TTIP) in ammonia alcoholic solution. We use alcohol and NH_4Cl to tune the reactivity of TTIP and the growth kinetics of TiO_2 to control the structural and morphological evolution. To demonstrate the intrinsic role of the 1D nanostructure, electronic process parameters such as charge transport, interfacial charge transfer, and particularly the trap-free diffusion coefficient of charges in TiO_2-based electrochemical systems were investigated. The I^-/I_3^- redox couple system was adopted to study the electrochemical behavior of the 1D TiO_2

dx.doi.org/10.1021/ja5080568 | J. Am. Chem. Soc. 2014, 136, 15310−15318

nanostructures, as iodine is one of the most ideal redox couples with appropriate conversion kinetics in heterogeneous charge transfer,[21,22] which has been widely used in DSSCs.[9,10]

EXPERIMENTAL SECTION

Synthesis of Anatase Nanorods. Anatase nanorods (AlAR) were synthesized by the one-step hydrothermal treatment of the titanium alkoxide precursor in ammonia solution. In a typical synthesis, 0.8 g of NH_4Cl (Merck) was first dissolved in 8 mL of isopropyl alcohol (Pr^iOH, Fisher Scientific; assay >99.5%, water <0.2%) in a Teflon-lined stainless steel autoclave (50 mL). The mixture was stirred under ambient conditions for 5 min before the addition of 0.2 mL of titanium(IV) tetraisopropoxide (TTIP, Sigma-Aldrich, 97%). After the mixture was stirred for 30 min, 10 mL of ammonia (Kanto Chemical Co., 28−30% by weight) was added. After the mixture was stirred for another 5 min, the reactor was sealed and kept at 170 °C for 72 h. After the reaction, the resulting precipitates were collected and washed several times with deionized water and ethanol. Finally, the products were dried under vacuum at 60 °C for further use. The effect of the amount of alcohol (Pr^iOH, 0−20 mL), dosage of NH_4Cl (0−2 g), and the rate of hydrolysis of TTIP (realized by changing the charging sequence) were also investigated.

For comparison, conventional anatase nanorods (denoted NaAR) were also synthesized by the hydrothermal treatment of TiO_2 powder (P25, Degussa) in concentrated NaOH solution. Briefly, P25 powder (2 g) was dispersed into 100 mL of NaOH solution (10 M) in a Teflon-lined stainless steel autoclave with stirring. Afterward, the sealed autoclave was heated to 170 °C for 24 h. The collected precipitates were washed several times with water and dilute HCl. The final product was obtained by calcining the washed precipitates at 600 °C for 2 h. Anatase TiO_2 nanoparticles (ANP) were synthesized according to our previously reported procedure by hydrothermal synthesis starting from titanium(IV) *n*-butoxide.[23] Briefly, 40 mL of titanium(IV) *n*-butoxide was added dropwise into 240 mL of 0.1 M HNO_3 with vigorous stirring. Then, the obtained slurry was rapidly heated to 80 °C and kept at this temperature for 8 h. After peptization, the colloidal solution was transferred to a Teflon-lined autoclave and heated for 12 h to 230 °C to grow TiO_2 nanoparticles.

Fabrication of DSSCs. The TiO_2 pastes used for making DSSC electrodes were prepared by ultrasonically dispersing the as-prepared anatase nanostructures into an ethanol/water mixture (1/1 by volume). The mixed dispersion was then concentrated to a final TiO_2 concentration of ∼15 wt %. Afterward, polyethylene glycol (PEG, molecular weight 20000) was added with a proportion of 50% of the TiO_2 weight. The as-prepared pastes were deposited by the doctor-blade technique on fluorine-doped tin oxide conducting glass substrate (FTO, 14 Ω/square, Nippon Sheet Glass) with an active area of 0.38 cm^2. The film was then heated to 500 °C at a rate of 15 °C/min and kept at this temperature for 30 min. After it was cooled to 80 °C, the TiO_2 electrode was immersed overnight in an N719 dye (Solaronix) solution (0.5 mM in acetonitrile). The electrode was then rinsed with acetonitrile and dried. Afterward, one drop of iodine-containing electrolyte was deposited onto the surface of the electrode and it penetrated inside the TiO_2 film via capillary action. The electrolyte was composed of 0.1 M of lithium iodide (LiI, Sigma-Aldrich), 0.6 M of tetrabutylammonium iodide (TBAI, Sigma-Aldrich), 0.05 M of iodine (I_2, Sigma-Aldrich), and 0.5 M of 4-*tert*-butylpyridine (*t*BP, Sigma-Aldrich) that was dissolved in acetonitrile. A platinized FTO counter electrode was then clipped onto the top of the TiO_2 photoelectrode to form photovoltaic devices.

Photoelectrochemistry and Electrochemistry. The photovoltaic properties of DSSCs were characterized by recording the photocurrent−voltage (*J*−*V*) curves under AM 1.5 G illumination (100 mW/cm^2). The illumination was provided by a Newport-Oriel solar simulator. Electrochemical impedance measurements of the cells were performed with a computer-controlled Solartron potentiostat with a frequency of 0.05−500 kHz; the amplitude of the ac signal was 10 mV. The obtained spectra were fitted with Z-view software. To determine the flat band potential of the semiconductor electrodes, Mott−Schottky plots were obtained by performing potentiodynamic electrochemical impedance spectroscopy.

Materials Characterization. The TiO_2 nanostructures were characterized by X-ray diffraction (XRD) using a Bruker D8 X-ray powder diffractometer. Transmission electron microscopy (TEM) and high-resolution TEM (HRTEM) investigations were taken with a JEOL JEM-3010 field emission electron microscope operated at 300 kV. The selected area electron diffraction (SAED) pattern of the samples was obtained by fast Fourier transform of the HRTEM image using DigitalMicrograph software (Gatan). The morphologies of the samples were characterized by field emission scanning electron microscopy (FESEM) carried out on a JEOL JSM-6701F electron microscope. The amount of dye uptake on the semiconductor electrodes was measured by dye desorption in ethanolic solution containing 0.1 M NaOH. The absorbance of the resulting solution was measured by UV−visible spectrophotometry (Varian Cary 4000).

RESULTS AND DISCUSSION

Synthesis and Characterization of TiO_2 Nanostructures. The as-synthesized TiO_2 nanorods (AlAR) are phase-pure anatase with an average diameter of ∼50 nm and lengths of several hundred nanometers (Figure 1a,b). As observed from the FESEM images (Figure 1a and Figure S1 (Supporting Information)), the TiO_2 nanorods have a pyramidal shape with sharp edges extending along the axial direction to the tip of the quadrangular. Different from the standard powder X-ray diffraction (XRD) pattern, the XRD profile of the as-synthesized TiO_2 nanorods displays a relatively intense and narrow (004) diffraction peak (Figure 1b and Figure S2 (Supporting Information)), suggesting that the 1D nanorods are single crystalline with the preferred growth direction. TEM and HRTEM analyses show that the nanorods are indeed single crystalline and have a distorted-tetragonal shape in the tip without central symmetry to the axis (Figure 1c,d). The angles in the tip are 43 and 137°, which can be attributed to the angle and supplementary angle between the (101) and (−101) planes, respectively (Figure 1e,f).

The formation of TiO_2 undergoes the following two steps: hydrolysis of titanium alkoxide and polycondensation of hydroxyalkoxides. To obtain TiO_2 nanostructures with regular morphologies, it is desirable to tune the growth procedure through thermodynamics rather than kinetics. In our system, the hydrolysis of TTIP was kinetically suppressed by introducing isopropyl alcohol (Pr^iOH) into the growth medium to shift the chemical reaction equilibrium, which was explained by the chemical reaction[24]

$$\mathrm{Ti(OR)_4} + x\mathrm{H_2O} \overset{\mathrm{ROH}}{\longleftrightarrow} \mathrm{Ti(OH)}_x\mathrm{(OR)}_{4-x} + x\mathrm{ROH}$$

$$K_j = \prod_{i=1}^{j} \frac{[\mathrm{Ti(OR)}_{4-i}\mathrm{(OH)}_i][\mathrm{ROH}]}{[\mathrm{Ti(OR)}_{5-i}][\mathrm{H_2O}]} \quad (1)$$

in which K_j is the overall equilibrium constant for the hydrolysis reaction through multiple hydrolysis steps (i.e., j = 1−4). In addition, the introduction of a small amount of NH_4Cl in the growth solution can reduce the nucleophilicity of water and further slow the hydrolysis of TTIP. Prior to the addition of ammonia into the growth solution, the concentration of water in the growth solution is very low (<0.2 wt % in Pr^iOH) and precipitation of titanium alkoxide from fast hydrolysis could be prevented, which gives titanium alkoxide molecules adequate time to homogeneously release the alkoxy groups. As a result, $Ti(OR)_3(OH)$ could be the predominant hydrolyzed products. In contrast, fast hydrolysis of titanium alkoxide results

dx.doi.org/10.1021/ja5080568 | J. Am. Chem. Soc. 2014, 136, 15310−15318

undesirably in precipitation of the titanium species, leading to the formation of isotropic TiO_2 nanoparticles after a hydrothermal reaction (Figure S3 (Supporting Information)).

After partial hydrolysis, polymerization of the hydrolyzed alkoxides took place prior to the addition of ammonia–water. Owing to the positive partial charge on Pr^iOH, alcoxolation between hydroxyalkoxide molecules should be favored thermodynamically, resulting in the formation of 1D titanium polymer chains, which we believe is critical in promoting 1D growth of TiO_2 nanorods in the subsequent hydrothermal reaction:[24]

$$n\mathrm{Ti(OPr^i)_3(OH)} \rightarrow \cdots\mathrm{-O-Ti(OPr^i)_2-O-}\cdots + n\mathrm{Pr^iOH} \quad (2)$$

On the basis of this relationship (eq 2), the polymerization of the hydrolyzed alkoxides should be affected by the ratio of parent alcohol to TTIP in the starting solution (Figure S4 (Supporting Information)). It can be seen from Figure S4a–f that 1D nanostructures become predominant as the addition of Pr^iOH increases. However, by further increasing the ratio of Pr^iOH to TTIP, the lowering of the concentration of hydroxyalkoxides would prevent the formation of large enough titanium polymeric chains, which would in turn negatively affect the 1D growth of TiO_2 nanorods (Figure S4g,h).

The addition of NH_4Cl is also critical in influencing the 1D evolution of TiO_2 nanorods during the hydrothermal reaction (Figure S5 (Supporting Information)). In our system, NH_4Cl plays multiple roles in promoting the 1D growth of anatase nanorods. In addition to adjusting the hydrolysis rate of titanium alkoxide (prior to addition of ammonia–water), it can also modify the reaction kinetics of the oxo-alkoxides by attaching and/or detaching the chlorine ions on the TiO_2 surface,[25,26] thus promoting the 1D growth of anatase nanorods. Therefore, during the thermodynamically controlled process of the hydrothermal reaction, the long-lasting (72 h), high-temperature (170 °C) treatment can tune the growth reactivity to expose the lowest energy surface of anatase (101) and facilitate the 1D evolution.

Ammonia–water plays an indispensable role in our system to promote the growth of 1D anatase nanorods. It is generally accepted that formation of anatase TiO_2 is favored in alkaline medium because of the presence of excess hydroxyl species.[27] Here in our system, the introduction of ammonia–water not only helps to grow the TiO_2 nanostructures into the desired anatase phase[27] but also influences the morphology of the final hydrothermal products. When ammonia was absent, only irregular and polydispersed TiO_2 microspheres were synthesized (Figure S6 (Supporting Information)). By introducing ammonia–water into the reaction system, the morphologies of the hydrothermal products evidently changed. It can be seen that an increase in the concentration of ammonia is favorable to grow longer TiO_2 nanorods with larger aspect ratios (Figure S6). The formation route for 1D anatase nanostructures is schematically illustrated in Figure 2.

Intrinsic Superiority of Dimensionality of One-Step Synthesized Anatase Nanorods. *Impedance Spectroscopy Results.* To illustrate the importance of intrinsic superiority of dimensionality in photoelectrochemical systems, the electronic processes occurring in nanorod electrodes (Figure S7 (Supporting Information)) assembled from AlAR and anatase TiO_2 nanorods synthesized in concentrated NaOH solution (NaAR, Figure S8 (Supporting Information)) were investigated by electrochemical impedance spectroscopy. For cells with

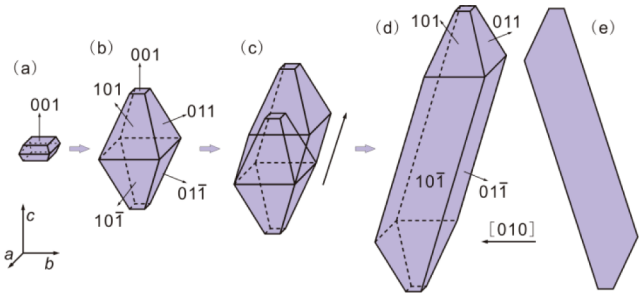

Figure 2. Schematic illustrations of the formation route of 1D anatase nanostructures. (a–d) During the hydrothermal reaction, the nanostructures gradually lose the exposed high-energy surfaces such as the (001) and (100) planes and only expose surfaces with the lowest surface energy—the (101) plane. It can be seen that the tip of the spatial structure in (d) is very similar to the morphology of nanostructures shown in the FESEM images (Figure 1a and Figure S1 (Supporting Information)). (e) is the projection of the crystal shown in (d) viewed along the [010] axis, which is very similar to the TEM images shown in Figure 1c,d.

good carrier collection efficiencies, electron transport in TiO_2 films appears as Warburg-like diffusion behavior in the high-frequency range and the interfacial charge recombination process grows into a large semicircle in the low-frequency region.[28] Figure 3a shows the Nyquist diagrams of the cells at

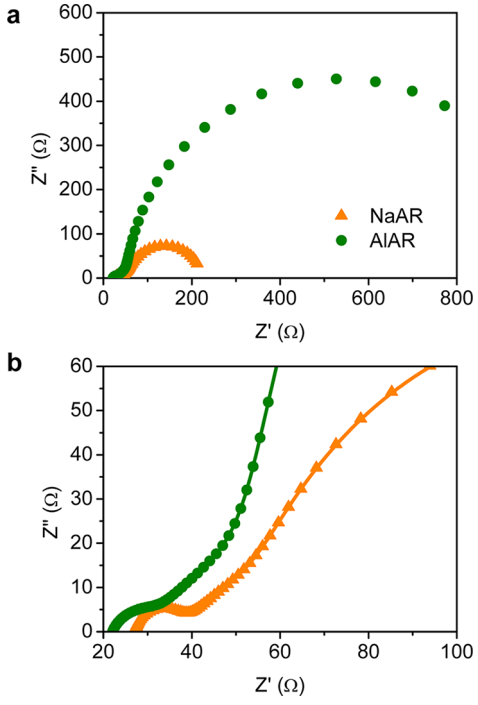

Figure 3. (a) Nyquist diagrams of the impedance spectra of cells measured at a bias of −700 mV. (b) Magnification of the high-frequency region of plots in (a).

potentials where the two semiconductor electrodes have similar electron transport resistances (as magnified in Figure 3b). In this situation, it is observed that the interfacial charge transfer resistance is much larger for the AlAR electrode than for the NaAR device, indicating that the one-step synthesized anatase nanorods can effectively save the electrons from recombination with the oxidized species: e.g., I_3^- in the electrolyte.

dx.doi.org/10.1021/ja5080568 | J. Am. Chem. Soc. 2014, 136, 15310–15318

The electronic processes in a DSSC are well described by the transmission line model developed by Bisquert et al. (Figure S9 (Supporting Information)).[28−31] Upon forward bias, electrons are injected from the FTO substrate into TiO_2 and the film is charged by electron propagation through the TiO_2 network. Meanwhile, a fraction of the injected conduction band electrons are lost by reacting with the I_3^- ions in the electrolyte.[32] By fitting impedance data with the transmission line, we obtained parameters including the electron transport resistance (R_t), the interfacial charge recombination resistance (R_{ct}), and chemical capacitance (C_μ), which describe the electronic processes in DSSCs.

It has been established that the conductivity of the electrons in the TiO_2 network is exclusively dependent on the number of free electrons in the extended states:[33] $\sigma = e\mu n$ (where e is the elementary charge and μ is the mobility). Thus, electron conductivity provides a reference for the position of the electronic Fermi level (E_F) with respect to the conduction band edge (E_{CB}) of TiO_2[33,34]

$$\sigma = \sigma_0 \exp\left[\frac{E_F - E_{CB}}{k_B T}\right] \quad (3a)$$

where σ_0 is a constant, k_B is the Boltzmann constant, and T is the temperature. Since σ_0 relates only to the steady-state transport and reflects the rate of displacement in the transport band, the electron conductivity in a multiple trapping scheme is independent of the number of traps.[35] In contrast, the electron diffusion coefficient of the semiconductor network is strongly dependent on the occupation of traps.[14] Thus, it is reasonable to take the electron conductivity as a parameter to compare the electrochemical properties of different semiconductor electrodes. The conductivity of the TiO_2 network can be calculated from R_t by using the geometrical parameters.

In a DSSC, the redox potential (E_{redox}) of I^-/I_3^- in electrolyte is stationary. The bias potential of the cell is related to the difference between the electronic Fermi level in the TiO_2 and E_{redox} of I^-/I_3^-. Therefore, the relationship of potential to conductivity can provide us with the difference between E_{CB} of TiO_2 and E_{redox} of I^-/I_3^-:

$$\sigma = \sigma_0 \exp\left[\frac{e}{k_B T}\left(V + \frac{E_{redox} - E_{cb}}{e}\right)\right] \quad (3b)$$

Figure 4a presents the comparison of potential versus conductivity of the cells assembled from AlAR and NaAR. The plots of the two electrodes are distributed almost on the same line over the conductivity range, suggesting that the conduction band edges (E_{CB}) for NaAR and AlAR are nearly identical.

Recombination of electrons with I_3^- in the electrolyte cannot be ignored, due to the relatively slow transport of charge through the TiO_2 electrode. The recombination process always competes with the collection of electrons. The charge recombination on the SEI can be described by the R_{ct} value, which can be obtained from impedance results. Figure 4b shows the charge transfer resistance on the SEI of the two electrodes. By a comparison of the two curves, it is clear that electrons in the AlAR electrode can be more effectively suppressed from recombination because of greater charge transfer resistance. In addition, the higher slope of the curve for the AlAR electrode reveals that electron transfer intermediated by surface states is less predominant.

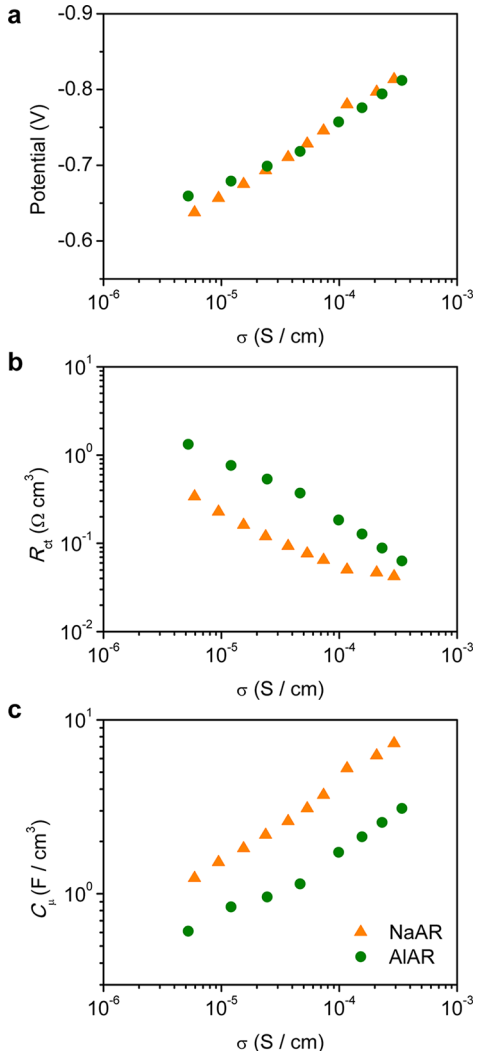

Figure 4. Impedance results for the cells assembled from conventionally prepared anatase nanorods (NaAR) and one-step synthesized anatase nanorods (AlAR): (a) electrode potential (electronic Fermi level); (b) charge recombination resistance; (c) chemical capacitance for the NaAR and AlAR electrodes varied over the measured conductivity range. The potential for each point (a) was corrected by *iR* drop.

The chemical capacitance is also affected by the preparation methods of TiO_2 (Figure 4c). In all measurement ranges, the capacitance of the NaAR electrode is about twice as large as that assembled from AlAR. The larger capacitance for the NaAR electrode indicates a higher density of electronic trap states below the conduction band edge of NaAR. There are many factors influencing the chemical capacitance of the TiO_2 network: e.g., lattice defects and uptake of protons. The uptake of protons into nanocrystalline TiO_2 has been demonstrated by Hupp and co-workers using a photoelectrochemical quartz crystal microbalance technique.[36,37] It was found that intercalation of cations into the TiO_2 lattice could result in a high density of intraband sites and therefore a great increase in the capacitance. Here in our case, the NaARs were prepared by deintercalation of sodium from the sodium titanate host. This procedure could produce large amounts of defects and crystalline distortions, which would increase the density of electronic states within the band gap of TiO_2.[28,38] The

dx.doi.org/10.1021/ja5080568 | J. Am. Chem. Soc. 2014, 136, 15310−15318

electronic states will later play a role as electronic traps during the operation of photovoltaic devices.

Charge Transport. Electron transport in DSSCs is mainly driven by diffusion, due to the effective electrolyte shielding of space charge.[14] The diffusion coefficient of the electrons within the mesoporous semiconductor electrodes strongly depends on the architectural construction and density and distribution of the trap states located in the band gap. The effective diffusion coefficient is given by[35]

$$D_n = \frac{1}{1 + \frac{\partial n_L}{\partial n_C}} D_0 \tag{4a}$$

where n_L is the trapped electron density and n_C is the conduction band electron density. When $E_F < E_{CB} - k_B T$, the term $\partial n_C/\partial n_L$ is small; then eq 4a becomes

$$D_n = \left(\frac{\partial n_C}{\partial n_L}\right) D_0 \tag{4b}$$

The prefactor $\partial n_C/\partial n_L$ reflects the delay of the response of the chemical diffusion coefficient by the trapping and detrapping processes. D_0 is the constant diffusion coefficient of freely mobile electrons (trap-free charge transport) at or above the transport edge of the semiconductor mesoporous electrodes, which is closely related to the architectural construction.[39] Thus, the value of D_0 would be a characteristic parameter for a given semiconductor electrode, which provides insight into important information about construction associated with the structural disorder, the crystallite (grain) size, the coordination number, and the necking condition of interparticle connections for a given cell. The measurement of chemical diffusion coefficient can be done through

$$D_n = \frac{N_C T_0}{N_L T} \exp\left[(E_F - E_C)\cdot\left(\frac{1}{k_B T} - \frac{1}{k_B T_0}\right)\right] D_0 \tag{4c}$$

where N_C is the effective density of states in the conduction band, N_L is the total density of the localized states, and T_0 is the characteristic temperature which determines the depth and distribution of trap sites below the lower edge of the conduction band. When $E_F \approx E_{CB} - k_B T$, the term $\partial n_C/\partial n_L \geq 1$; in this situation, the chemical diffusion coefficient of charge is equal to the constant diffusion coefficient ($D_n \approx D_0$, according to eq 4a). The constant diffusion coefficient can be estimated by extrapolating the D_n–E_F relationship obtained at various temperatures.[40]

In DSSCs, the electron transport depends strongly on light intensity and/or the electrode potential, due to the broad distribution of band gap traps.[41] The simplest approach to take trapping into consideration is the classical multiple trapping (MT) framework,[42,43] which has been applied to DSSCs and other types of photoelectrochemical cells.[44−47] In this model, transport of electrons through extended states is slowed down by trapping/detrapping events, while direct hopping between localized states is neglected.[35,42−48] The waiting time for the thermal release of electrons to the extended state strongly influences the time constant of charge transport.

It is therefore elicited that the effective electron diffusion coefficient (D_n) is governed by the density of localized states and the depth of the trap sites. Under quasi-steady-state conditions, the effective diffusion coefficient of the electron in the TiO_2 electrode can be obtained by using small perturbation techniques such as intensity modulated photocurrent spectroscopy (IMPS) and impedance spectroscopy. Here we calculated D_n from the transport resistance, R_t, and chemical capacitance, C_μ, on the basis of $D_n = (R_t C_\mu)^{-1}$. It was found that the value of D_n for AlAR is more than twice as large as that for NaAR (Figure 5).

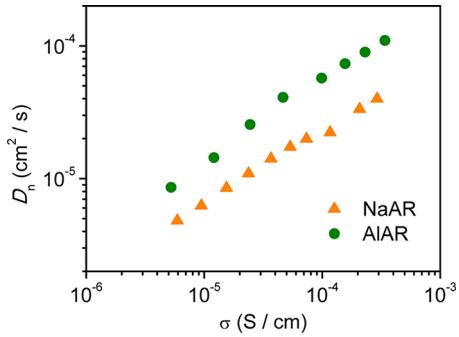

Figure 5. Electron diffusion coefficient for the NaAR and AlAR electrodes varied over the measured conductivity range.

On the basis of the MT model, D_n grows exponentially as E_F shifts toward more negative potential. The charge transport activation energy and constant diffusion coefficient can be obtained by investigating the chemical diffusion coefficient at various temperatures.[39,49] Figure 6 shows the exponential variation of D_n values over the electronic Fermi level at various temperatures. The estimated D_0 for the AlAR electrode reaches as high as 0.092 cm^2/s, which is much larger than the values obtained from the nanoparticle films (refs 50 and 51 and Figure S10 (Supporting Information)). In contrast, even though the construction and building blocks of the NaAR electrode are similar to those of AlAR, the D_0 value is as low as 0.0043 cm^2/s, which is only twice that of the electrode made of nanoparticles (0.0019 cm^2/s; see Figure S10).

As mentioned earlier, the architectures of the mesoporous semiconductor electrode strongly influence the constant diffusion coefficient. The intercalation/deintercalation processes occurring during hydrothermal and post-treatment processes would introduce crystallographic defects. Since the ionic diffusion in the host lattice is relatively slow, introduction of "internal boundaries" such as domain wall cannot be avoided during the multiple (de)intercalation processes.[52] Domain structures are rather common in intercalation compounds such as graphite intercalation compounds and titanates,[53,54] and they becomes more evident as the size of the host increases. These phenomena have recently been confirmed by investigating the effects of particle size on the thermodynamics of lithium intercalation into anatase TiO_2.[55] The nonuniform distribution of the guest ions in the host inevitably produces boundary (lattice) strain. Here in our case, the multiple (de)intercalation of alkali-metal (and/or proton) ions in the TiO_2 host could generate lattice strain during the formation processes, which could not be neglected even after heat treatment of the samples. The residual strain would further influence the ion exchange and the dehydration processes. One of the common phenomena is that the 1D nanostructures can be cut into short analogues and even 0D nanoparticles by hydrothermal treatment of titanate nanorods (or nanowires).[56−58] This approach has now widely been employed as an efficient technique to prepare TiO_2 polyhedrons.[57,58] We noted that our 1D intermediates (sodium titanate and hydrogen titanate) could also be cut and converted into short nanorods by

dx.doi.org/10.1021/ja5080568 | J. Am. Chem. Soc. 2014, 136, 15310−15318

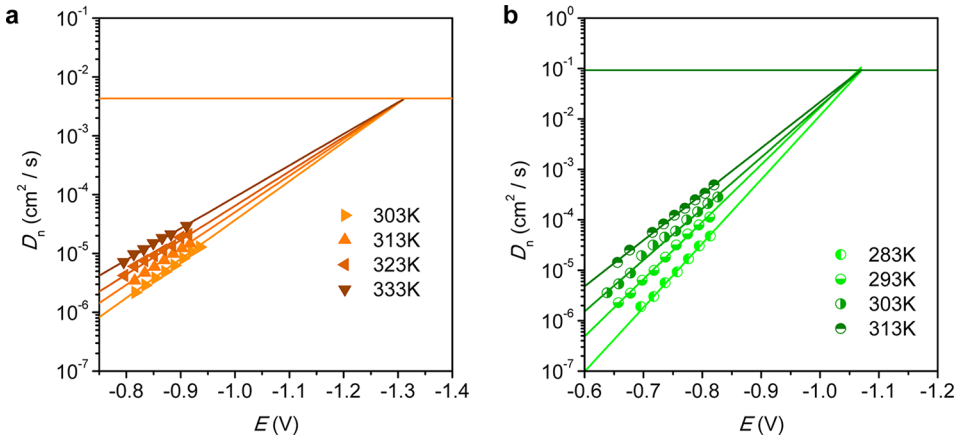

Figure 6. Electron diffusion coefficient for the NaAR (a) and AlAR (b) electrodes varied over the electronic Fermi level under various temperatures.

stressing long-term hydrothermal treatment (Figure S11 (Supporting Information)). In addition, we also found that the fwhm in the XRD pattern of NaAR is larger, in comparison with that of AlAR (Figure S12 (Supporting Information)), which indicates that the TiO_2 nanostructures prepared by multiple (de)intercalation processes possess obvious residual strain and/or smaller crystallite sizes. All of these features reveal that the 1D TiO_2 nanostructures synthesized from the corresponding titanate by multiple (de)intercalation processes followed by high-temperature dehydration are not truly *continuous*. The existence of grain boundaries in the *discontinuous* NaAR nanostructures will hinder the electronic process and lower the trap-free charge diffusion coefficient by grain scattering (Figure 6a and Figure 7). In contrast, an AlAR

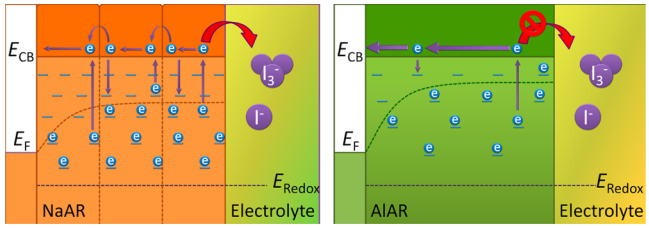

Figure 7. Features of the electronic processes occurring in photoelectrochemical cells (DSSCs) based on NaAR (left) and AlAR (right) electrodes. As illustrated in the figure, cells with AlAR electrodes have evident advantages over the NaAR electrode in charge transport and charge collection. This is due to the fact that the continuous AlAR nanostructures can reduce the electron scattering and increase the constant (trap-free) diffusion coefficient. Moreover, the lower density of trap sites in the band gap of the AlAR electrode reduces the trapping/detrapping events during charge transport, which will further increase the diffusion coefficient of electrons. In addition, the higher density of accumulated electrons resulting from the suppression of charge recombination on the SEI increases the filling of the traps, which also facilitates the charge transport.

electrode consisting of a boundaryless nanostructure can reduce the electronic scattering during the electronic processes, which is beneficial for charge transport and can increase the trap-free diffusion coefficient (Figure 6b and Figure 7).

By virtue of these benefits, the diffusion length of electrons (L_n) in the semiconductor electrodes can be effectively increased. The effective electron diffusion length can be obtained from the impedance data on the basis of

$$L_n = \sqrt{R_{ct}/R_t} = \sqrt{\sigma R_{ct}} \quad (5)$$

Figure 8 shows the values of L_n versus the conductivity of the semiconductor for the two electrodes. The AlAR electrode with

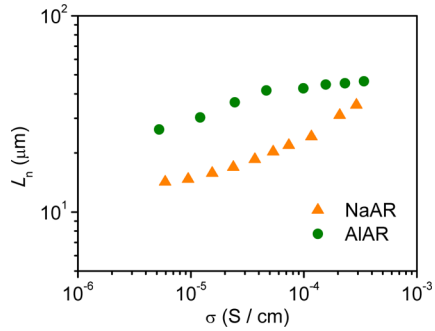

Figure 8. Effective electron diffusion length for the NaAR and AlAR electrodes varied over the measured conductivity range.

more efficient charge transport (Figures 5–7) and greater resistance for charge recombination (Figure 4b) shows much higher values of L_n over the entire measured conductivity range (Figure 8).

The values of L_n also reflect the competition between the electron transport and recombination of the charge on the semiconductor–electrolyte interface, which determines the collection efficiency of photogenerated charges during the operation of the DSSCs. The suppression of charge transfer on the SEI for AlAR can increase the filling of trap states and further facilitate charge transport by reducing the number of trapping/detrapping events (Figures 5 and 7). Thus, it is expected that the DSSCs composed of AlAR electrodes with a relatively lower density of trap states in the band gap can exhibit higher photocurrent.

Photovoltaic Characteristics. The photocurrent–voltage (J–V) features (Figure 9) show that the DSSCs assembled from NaAR electrodes deliver a short-circuit photocurrent density (J_{SC}) of 11.80 mA/cm^2, an open-circuit voltage (V_{OC}) of 782 mV, a fill factor (FF) of 0.616, and thus an energy conversion efficiency (η) of 5.68%. By replacement of the NaAR electrode with an AlAR electrode, the values for J_{SC} and V_{OC} increased to 17.05 mA/cm^2 and 785 mV, respectively, with an energy conversion efficiency of 7.80%.

Photocurrent is a function of light harvesting, electron injection, and charge collection. As determined from the dye

dx.doi.org/10.1021/ja5080568 | J. Am. Chem. Soc. 2014, 136, 15310–15318

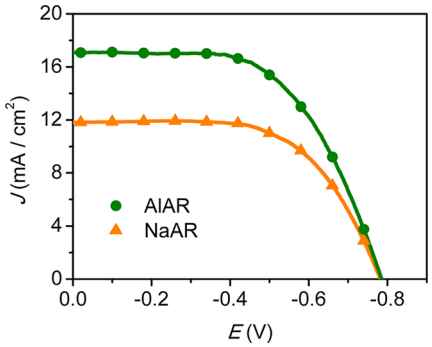

Figure 9. Photovoltaic characteristics of the DSSCs assembled from NaAR and AlAR electrodes. The detailed photovoltaic parameters, including open-circuit voltage (V_{OC}), short-circuit photocurrent density (J_{SC}), fill factor (FF), and overall energy conversion efficiency (η) are 782 mV, 11.80 mA/cm^2, 0.616, and 5.68% for the NaAR DSSC and 785 mV, 17.05 mA/cm^2, 0.583, and 7.80% for the AlAR DSSC, respectively.

desorption measurements, the amount of adsorbed dye on the NaAR electrode is slightly higher than that on the AlAR electrode (Figure S13 (Supporting Information)). In addition, the injection efficiency of photogenerated electrons from the dye molecules to the semiconductor should be identical for AlAR and NaAR, as the conduction band edges of the two electrodes have nearly the same position, as determined by the relationship between the potential and conductivity, as well as the flat band potential obtained from the Mott−Schottky measurement (Figure 4a and Figure S14 (Supporting Information)). Therefore, the increase in values of J_{SC} and V_{OC} for the DSSCs assembled from AlAR could be conclusively ascribed to the improved electron collection and suppressed charge recombination (Figures 4b, 7, and 8).

CONCLUSIONS

In summary, we have demonstrated a novel strategy to thermodynamically promote 1D evolution of anatase TiO_2 nanostructures via a suitable control of reaction kinetics. Guided by our strategy, we have successfully synthesized single-crystalline 1D anatase nanorods by a one-step hydrothermal reaction. The synthesized anatase nanorods with a lower density of electronic traps and continuous structures can reduce trapping/detrapping events and grain scattering, which enables the emergence of the intrinsic superiority of dimensionality over the conventional anatase counterparts by showing more efficient charge transport and collection, as well as higher energy conversion efficiency in photoelectrochemical devices.

ASSOCIATED CONTENT

Supporting Information

Figure S1−S14, as described in the text. This material is available free of charge via the Internet at http://pubs.acs.org.

AUTHOR INFORMATION

Corresponding Author

*E-mail for b.L.: liubin@ntu.edu.sg.

Notes

The authors declare no competing financial interest.

ACKNOWLEDGMENTS

The authors acknowledge Nanyang Technological University (M4080977.120), the Ministry of Education of Singapore (M4011021.120), A*Star (M4070178.120), and the Singapore-Berkeley Research Initiative for Sustainable Energy (SinBeRISE) for financial support. J.C. thanks Dr. Yinghua Xu (Zhejiang University of Technology) and Dr. Tiancheng Xu (HzCell Electrochemical Corp.) for help in the discussion of impedance results.

REFERENCES

(1) Law, M.; Greene, L. E.; Johnson, J. C.; Saykally, R.; Yang, P. *Nat. Mater.* **2005**, *4*, 455.
(2) Huang, M. H.; Mao, S.; Feick, H.; Yan, H.; Wu, Y.; Kind, H.; Weber, E.; Russo, R.; Yang, P. *Science* **2001**, *292*, 1897.
(3) Xia, Y.; Yang, P.; Sun, Y.; Wu, Y.; Mayers, B.; Gates, B.; Yin, Y.; Kim, F.; Yan, H. *Adv. Mater.* **2003**, *15*, 353.
(4) Liu, C.; Tang, J.; Chen, H. M.; Liu, B.; Yang, P. *Nano Lett.* **2013**, *13*, 2989.
(5) Chen, X.; Shen, S.; Guo, L.; Mao, S. S. *Chem. Rev.* **2010**, *110*, 6503.
(6) Yin, Y.; Talapin, D. *Chem. Soc. Rev.* **2013**, *42*, 2484.
(7) Chen, X.; Mao, S. S. *Chem. Rev.* **2007**, *107*, 2891.
(8) Fujishima, A.; Honda, K. *Nature* **1972**, *238*, 37.
(9) Gratzel, M. *Nature* **2001**, *414*, 338.
(10) Oregan, B.; Gratzel, M. *Nature* **1991**, *353*, 737.
(11) Liu, B.; Aydil, E. S. *J. Am. Chem. Soc.* **2009**, *131*, 3985.
(12) Hwang, Y. J.; Hahn, C.; Liu, B.; Yang, P. *ACS Nano* **2012**, *6*, 5060.
(13) Liu, B.; Chen, H. M.; Liu, C.; Andrews, S. C.; Hahn, C.; Yang, P. *J. Am. Chem. Soc.* **2013**, *135*, 9995.
(14) Bisquert, J. *Phys. Chem. Chem. Phys.* **2008**, *10*, 49.
(15) Park, N. G.; van de Lagemaat, J.; Frank, A. J. *J. Phys. Chem. B* **2000**, *104*, 8989.
(16) Chen, J.; Li, B.; Zheng, J.; Jia, S.; Zhao, J.; Jing, H.; Zhu, Z. *J. Phys. Chem. C* **2011**, 7104.
(17) Tsai, C.-C.; Teng, H. *Chem. Mater.* **2005**, *18*, 367.
(18) Kitano, M.; Wada, E.; Nakajima, K.; Hayashi, S.; Miyazaki, S.; Kobayashi, H.; Hara, M. *Chem. Mater.* **2013**, *25*, 385.
(19) Riss, A.; Elser, M. J.; Bernardi, J.; Diwald, O. *J. Am. Chem. Soc.* **2009**, *131*, 6198.
(20) Zhu, K.; Neale, N. R.; Miedaner, A.; Frank, A. J. *Nano Lett.* **2007**, *7*, 69.
(21) Svensson, P. H.; Kloo, L. *Chem. Rev.* **2003**, *103*, 1649.
(22) Boschloo, G.; Hagfeldt, A. *Acc. Chem. Res.* **2009**, *42*, 1819.
(23) Chen, J.; Li, B.; Zheng, J.; Zhao, J.; Jing, H.; Zhu, Z. *Electrochim. Acta* **2011**, *56*, 4624.
(24) Livage, J.; Henry, M.; Sanchez, C. *Prog. Solid State Chem.* **1988**, *18*, 259.
(25) Barnard, A. S.; Curtiss, L. A. *Nano Lett.* **2005**, *5*, 1261.
(26) Yang, H. G.; Sun, C. H.; Qiao, S. Z.; Zou, J.; Liu, G.; Smith, S. C.; Cheng, H. M.; Lu, G. Q. *Nature* **2008**, *453*, 638.
(27) Testino, A.; Bellobono, I. R.; Buscaglia, V.; Canevali, C.; D'Arienzo, M.; Polizzi, S.; Scotti, R.; Morazzoni, F. *J. Am. Chem. Soc.* **2007**, *129*, 3564.
(28) Fabregat-Santiago, F.; Bisquert, J.; Garcia-Belmonte, G.; Boschloo, G.; Hagfeldt, A. *Sol. Energy Mater. Sol. Cells* **2005**, *87*, 117.
(29) Bisquert, J. *J. Phys. Chem. B* **2001**, *106*, 325.
(30) Fabregat-Santiago, F.; Garcia-Belmonte, G.; Bisquert, J.; Zaban, A.; Salvador, P. *J. Phys. Chem. B* **2002**, *106*, 334.
(31) Fabregat-Santiago, F.; Bisquert, J.; Palomares, E.; Otero, L.; Kuang, D. B.; Zakeeruddin, S. M.; Gratzel, M. *J. Phys. Chem. C* **2007**, *111*, 6550.
(32) Wang, Q.; Moser, J. E.; Gratzel, M. *J. Phys. Chem. B* **2005**, *109*, 14945.
(33) Abayev, I.; Zaban, A.; Fabregat-Santiago, F.; Bisquert, J. *Phys. Status Solidi* **2003**, *196*, R4.

(34) Fabregat-Santiago, F.; Bisquert, J.; Cevey, L.; Chen, P.; Wang, M. K.; Zakeeruddin, S. M.; Gratzel, M. *J. Am. Chem. Soc.* **2009**, *131*, 558.
(35) Bisquert, J.; Vikhrenko, V. S. *J. Phys. Chem. B* **2004**, *108*, 2313.
(36) Yan, S. G.; Hupp, J. T. *J. Phys. Chem.* **1996**, *100*, 6867.
(37) Lemon, B. I.; Hupp, J. T. *J. Phys. Chem.* **1996**, *100*, 14578.
(38) Kavan, L.; Kalbáč, M.; Zukalová, M.; Exnar, I.; Lorenzen, V.; Nesper, R.; Graetzel, M. *Chem. Mater.* **2004**, *16*, 477.
(39) Villanueva-Cab, J.; Jang, S.-R.; Halverson, A. F.; Zhu, K.; Frank, A. J. *Nano Lett.* **2014**, *14*, 2305.
(40) Bisquert, J. *J. Phys. Chem. C* **2007**, *111*, 17163.
(41) Schwarzburg, K.; Willig, F. *Appl. Phys. Lett.* **1991**, *58*, 2520.
(42) Tiedje, T.; Cebulka, J. M.; Morel, D. L.; Abeles, B. *Phys. Rev. Lett.* **1981**, *46*, 1425.
(43) Orenstein, J.; Kastner, M. *Phys. Rev. Lett.* **1981**, *46*, 1421.
(44) Fisher, A. C.; Peter, L. M.; Ponomarev, E. A.; Walker, A. B.; Wijayantha, K. G. U. *J. Phys. Chem. B* **2000**, *104*, 949.
(45) Gonzalez-Vazquez, J. P.; Anta, J. A.; Bisquert, J. *J. Phys. Chem. C* **2010**, *114*, 8552.
(46) Leng, W. H.; Barnes, P. R. F.; Juozapavicius, M.; O'Regan, B. C.; Durrant, J. R. *J. Phys. Chem. Lett.* **2010**, *1*, 967.
(47) van de Lagemaat, J.; Frank, A. J. *J. Phys. Chem. B* **2000**, *104*, 4292.
(48) Bisquert, J. *J. Phys. Chem. B* **2004**, *108*, 2323.
(49) Wang, Q.; Ito, S.; Gratzel, M.; Fabregat-Santiago, F.; Mora-Sero, I.; Bisquert, J.; Bessho, T.; Imai, H. *J. Phys. Chem. B* **2006**, *110*, 25210.
(50) Kroeze, J. E.; Savenije, T. J.; Warman, J. M. *J. Am. Chem. Soc.* **2004**, *126*, 7608.
(51) Hendry, E.; Koeberg, M.; O'Regan, B.; Bonn, M. *Nano Lett.* **2006**, *6*, 755.
(52) Wagemaker, M.; Mulder, F. M. *Acc. Chem. Res.* **2012**, *46*, 1206.
(53) Ulloa, S. E.; Kirczenow, G. *Phys. Rev. Lett.* **1985**, *55*, 218.
(54) Dimiev, A. M.; Ceriotti, G.; Behabtu, N.; Zakhidov, D.; Pasquali, M.; Saito, R.; Tour, J. M. *ACS Nano* **2013**, *7*, 2773.
(55) Wagemaker, M.; Borghols, W. J. H.; Mulder, F. M. *J. Am. Chem. Soc.* **2007**, *129*, 4323.
(56) Li, J.; Xu, D. *Chem. Commun.* **2010**, *46*, 2301.
(57) Li, J.; Cao, K.; Li, Q.; Xu, D. *CrystEngComm* **2012**, *14*, 83.
(58) Li, J.; Yu, Y.; Chen, Q.; Li, J.; Xu, D. *Cryst. Growth Des.* **2010**, *10*, 2111.